function for the ground state, as well as recent estimates (*8*, *9*) are in favor of there being vacancies at the 10^{-4} per site level, even in the pure crystal (SOM text). Repeated efforts by Clark *et al.* to grow perfect, pure, single crystals have always observed nonclassical rotational inertia (NCRI) on the 10^{-4} level relative to the classically expected value (*10*), and this level or higher has been confirmed by others (*11*–*13*). Simulations (*14*, *15*) performed using the path-integral Monte Carlo method have been claimed to prove the nonexistence of vacancies; however, among other difficulties the equivalent temperature in these simulations is well above the relevant temperature at which Bose condensation takes place. In any case, simulating 10^4 atoms well enough to find a single defect is beyond the capabilities of those methods. I used a background density ($|\Psi|^2$) relative to the solid for pure ^{4}He) of 2×10^{-4} to 3×10^{-4}, which fixes μ in terms of g.

I assumed m^* to be fairly light relative to that of a helium atom (m_{He}) and used an estimate that is often quoted,$1/3m_{He}$ (other estimates are even smaller). This effective mass is such that the uncertainty energy that is necessary to localize the mass on a single site is on the order of 10 K. This is the same magnitude as estimates in (*10*) of the energy cost of a vacancy and suggests that those estimates may not have taken into account the kinetic energy that could be gained by delocalization. Regarding vacancies classically as strictly local configurations of the lattice is not reasonable.

m^* and the density of the boson field allow an estimate of the superfluid transition temperature from the Bose-Einstein equation

$$k_B T_c = \frac{2\pi\hbar^2}{m^*}\left(\frac{N}{2.61V}\right)^{2/3} \quad (3)$$

where N/V is the vacancy density, k_B is Boltzmann's constant, and T_c is the transition temperature.

By entering into Eq. 3 a typical solid density, a vacancy concentration of 2×10^{-4} to 3×10^{-4} per site, and a mass of $1/3m_{He}$, the resulting transition temperature is ~50 to 70 mK. This is very close to the transition temperature at which thermal hysteresis in the NCRI has been reported (*12*, *16*). I have discussed elsewhere (*17*) why reversible NCRI appears so far above T_c. One expects true superflow to be observable only below this T_c, if at all.

The parameter g, or equivalently the scattering length a, is not something one can accurately estimate. I next discuss here the consequences of assuming that g is reasonably small. This perhaps can be justified, again, from the fact that a light mass implies a somewhat extended lattice distortion. Here, I define a correlation length as

$$\xi = 1/\sqrt{8\pi n_0 a} \quad (4)$$

where $n_0 = |\Psi^2|$, which is the exponential decay length of a small perturbation in the vacancy field, according to Eq. 1. Given that $n_0 = 3 \times 10^{-4}$, even if a is a whole lattice constant, ξ is 10 lattice constants or 3 nm; it would be reasonable for ξ to be an order of magnitude larger. This is still not quite the scale at which the variation of surface-to-volume ratio in NCRI occurs (*18*), but almost.

What is of most interest is the effect of defects being attractive sites for vacancies. A dislocation core, for instance, is said to attract on the order of one vacancy per atomic length, calculated on the basis of localized high-energy vacancies (*19*). This amounts to a potential well in V that could be estimated as $VR^2 \approx 10$ to 15 K, where R is the well's radius. Balancing this against the repulsive interaction $g\Psi^4$, a dislocation core might be capable of attracting a cloud of $\propto 1/g$ vacancies with a radius on the order of ξ. Thus, the effect of dislocations can be somewhat magnified. Correspondingly, one would expect there to be similar diffuse densities of delocalized vacancies around grain boundaries and near surfaces. I would consider this to be one of the few possibile explanations for the degree to which crystal imperfection appears to enhance NCRI.

Why small concentrations of ^{3}He produce large effects remains an open question.

It seems possible to provide an accounting of most of the puzzling properties of low-temperature solid He by describing it as a Gross-Pitaevskii fluid of delocalized quantum vacancies. The idea that the superfluid is an intrinsic property of the pure crystal, which is locally enhanced by imperfections, seems to account for the low and reasonably invariant genuine superfluid transition and the large variations in the quantity of superflow, which otherwise appear to be irreconcilable.

References and Notes

1. E. Kim, M. H. W. Chan, *Phys. Rev. Lett.* **97**, 115302 (2006).
2. E. P. Gross, *Phys. Rev.* **106**, 161 (1957).
3. L. P. Pitaevskii, *Sov. Phys. JETP* **4**, 439 (1957).
4. A. F. Andreev, I. M. Lifshitz, *Sov. Phys. JETP* **29**, 1107 (1969).
5. P. Anderson, http://arXiv.org/abs/cond-mat/0504731 (2005).
6. L. Reatto, *Phys. Rev.* **183**, 334 (1969).
7. L. Reatto, G. V. Chester, *Phys. Rev.* **155**, 88 (1967).
8. M. Rossi, E. Vitali, D. E. Galli, L. Reatto, *J. Low Temp. Phys.* **153**, 250 (2008).
9. C. Cazorla, G. E. Astrakarchik, J. Casulleras, J. Boronat, http://arXiv.org/abs/0804.1851 (2008).
10. A. C. Clark, J. T. West, M. H. W. Chan, http://arXiv.org/abs/0706.0906v2 (2007).
11. A. Penzev, Y. Yasuta, M. Kubota, *J. Low Temp. Phys.* **148**, 677 (2007).
12. A. S. C. Rittner, J. Reppy, *Phys. Rev. Lett.* **97**, 165301 (2006).
13. Y. Aoki, J. C. Graves, H. Kojima, *Phys. Rev. Lett.* **99**, 015301 (2007).
14. N. Prokof'ev, B. Svistunov, *Phys. Rev. Lett.* **94**, 155302 (2005).
15. D. M. Ceperley, B. Bernu, *Phys. Rev. Lett.* **93**, 155303 (2004).
16. A. C. Clark, J. D. Maynard, M. H. W. Chan, http://arXiv.org/abs/0711.3619 (2007).
17. P. W. Anderson, *Phys. Rev. Lett.* **100**, 215301 (2008).
18. A. C. S. Rittner, J. Reppy, *Phys. Rev. Lett.* **98**, 175302 (2007).
19. L. Pollet *et al.*, *Phys. Rev. Lett.* **101**, 097202 (2008).

20. I acknowledge the hospitality of the Fondation des Treilles for the workshop in which this work was conceived and the lectures and valuable discussions of M. H. W. Chan, J. Beamish, L. Reatto, J. Dalibard, J. Boronat, S. Balibar, and J. Reppy at that workshop.

Supporting Online Material

www.sciencemag.org/cgi/content/full/324/5927/631/DC1
SOM Text
References

8 December 2008; accepted 2 March 2009
10.1126/science.1169456

Evidence for a Superglass State in Solid ^{4}He

B. Hunt,[1*] E. Pratt,[1*] V. Gadagkar,[1] M. Yamashita,[1,2] A. V. Balatsky,[3] J. C. Davis[1,4]†

Although solid helium-4 (^{4}He) may be a supersolid, it also exhibits many phenomena unexpected in that context. We studied relaxation dynamics in the resonance frequency $f(T)$ and dissipation $D(T)$ of a torsional oscillator containing solid ^{4}He. With the appearance of the "supersolid" state, the relaxation times within $f(T)$ and $D(T)$ began to increase rapidly together. More importantly, the relaxation processes in both $D(T)$ and a component of $f(T)$ exhibited a complex synchronized ultraslow evolution toward equilibrium. Analysis using a generalized rotational susceptibility revealed that, while exhibiting these apparently glassy dynamics, the phenomena were quantitatively inconsistent with a simple excitation freeze-out transition because the variation in f was far too large. One possibility is that amorphous solid ^{4}He represents a new form of supersolid in which dynamical excitations within the solid control the superfluid phase stiffness.

A "classic" supersolid (*1*–*5*) is a bosonic crystal with an interpenetrating superfluid component. Solid ^{4}He has long been the focus of searches for this state (*6*). To demonstrate its existence unambiguously, macroscopic quantum phenomena (*7*) such as persistent mass currents, circulation quantization, quantized vortices, or the superfluid Josephson effect must be observed. None of these effects have been detected in solid ^{4}He.

There are, however, indications that this material could be a supersolid. This is because high-Q torsional oscillators (TOs) containing solid ^{4}He exhibit an increase in resonance frequency

$f(T)$ at low temperatures. This is detectable below a temperature $T_C \sim 65$ mK in the purest, most crystalline samples; below $T_C \sim 300$ mK in more amorphous samples; and below at least $T_C \sim 500$ mK when dilute concentrations of ^{3}He exist (*8*–*11*). A strong dissipation peak in $D(T) \equiv Q^{-1}(T)$ occurs in association with the rapid rise of $f(T)$ (*9*, *10*, *12*), but their relation has not been explained. These results [now widely reproduced (*12*–*15*)] can be interpreted as a ^{4}He supersolid whose rotational inertia is reduced due to its superfluid component. Support for this interpretation comes from the reductions in the net frequency increase when the TO annuli containing solid ^{4}He are blocked (*9*, *16*).

But many phenomena inexplicable in the context of a classic superfluid are also observed in equivalent samples of solid ^{4}He. These include, for example, maximum dc mass flow rates inconsistent with the TO dynamics (*17*–*19*), large increases in T_C with the introduction of dilute ^{3}He concentrations (*8*, *11*), strong effects of annealing on the magnitude of TO frequency shifts (*12*, *20*), velocity hysteresis in the frequency shift (*13*), and shear stiffening of the solid coincident with the TO frequency increase (*21*). These phenomena indicate some unanticipated interplay between dynamical degrees of freedom of the solid and any superfluid component.

In response, new theories have been proposed that solid ^{4}He is (i) a nonsuperfluid glass (*22*, *23*), (ii) a fluid of fluctuating quantum vortices (*24*), (iii) a superfluid network at linked grain boundaries (*25*), (iv) a viscoelastic solid (*26*), or a superglass—a type of granular superfluid within an amorphous solid (*27*–*30*). To help discriminate between such ideas, we focus on the relaxation dynamics of solid ^{4}He, which should distinguish a simple superfluid state from a purely glassy state.

Using a TO containing solid ^{4}He (Fig. 1A), we measure $f(T)$ and $D(T)$ effects that are in good agreement with those of other research groups (*8*–*16*). Figure 1 shows the evolution of $f(T)$ (blue circles) and $D(T)$ (red triangles) for our typical sample; the change in $f(T)$ between 300 and 10 mK would represent a "supersolid fraction" of 4.8% if the frequency shift were entirely attributable to a superfluid decoupling. Our samples, while formed by the "blocked capillary" procedure and therefore amorphous, are of the type most widely studied in the field (*8*, *9*, *11*–*15*). Thus, they are representative of the full spectrum of solid ^{4}He effects to be explained. Equivalent effects were detected in four different samples studied in two different cells of this type (*31*). All our experiments were performed at a maximum wall velocity of less than 4.5 μm/s.

To examine the relaxational characteristics of solid ^{4}He, we perform the experiments outlined in fig. S1 (*31*). The temperature is decreased stepwise from an initial temperature T_i to a final equilibrium temperature T_{eq}, and the rapid coevolution of f and D is observed as the ther-

[1]Laboratory of Atomic and Solid State Physics, Department of Physics, Cornell University, Ithaca, NY 14853, USA. [2]Department of Physics, Kyoto University, Kyoto 606-8502, Japan. [3]T-Division, Center for Integrated Nanotechnologies, MS B 262, Los Alamos National Laboratory, Los Alamos, NM 87545, USA. [4]Scottish Universities Physics Alliance, School of Physics and Astronomy, University of St. Andrews, St. Andrews, Fife KY16 9SS, Scotland, UK.

*These authors contributed equally to this work.
†To whom correspondence should be addressed. E-mail: jcdavis@ccmr.cornell.edu

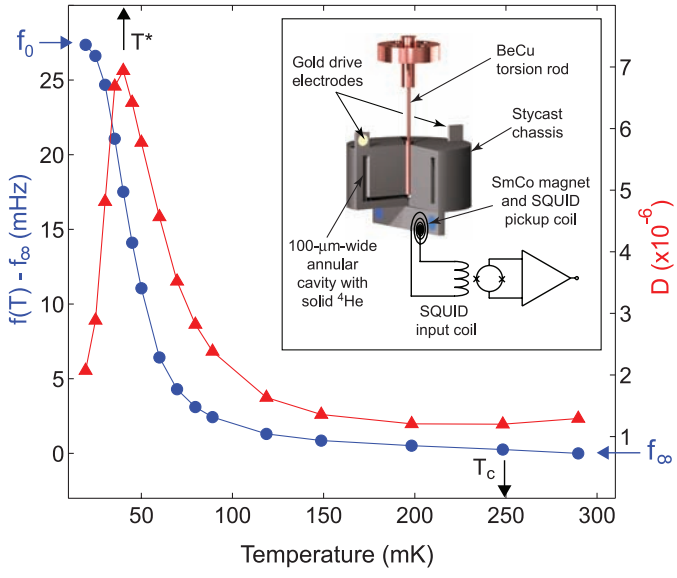

Fig. 1. The resonant frequency shift $f(T) - f_\infty$ (blue circles) and dissipation $D(T) \equiv Q^{-1}(T)$ (red triangles) for our TO-solid ^{4}He system. Indicated with black arrows are T^*, the temperature at which $D(T)$ peaks and the slope of $f(T) - f_\infty$ is maximal, and T_c, the temperature at which a change in $f(T) - f_\infty$ becomes detectable above the noise. (**Inset**) A schematic of the superconducting quantum interference device (SQUID)–based torsional oscillator (TO). Applying an ac voltage to the drive electrodes rotates the Stycast chassis (containing the solid ^{4}He in a 100-μm-wide annular cavity of radius 4.5 mm) about the axis of the BeCu torsion rod. The angular displacement of a SmCo magnet mounted on the TO generates a change in the magnetic flux through the stationary pickup and input coils of a dc-SQUID circuit and thereby a voltage proportional to displacement.

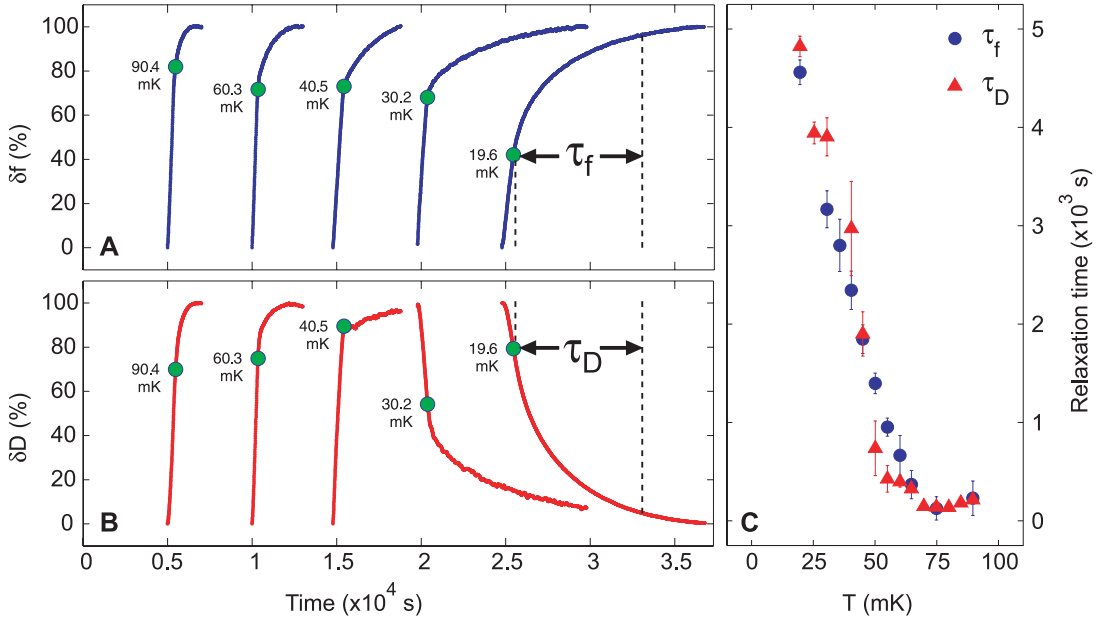

Fig. 2. Measured traces of (**A**) $f(t,T)$ and of (**B**) $D(t,T)$ for the stepwise-cooling experiment described in the text and fig. S1. These traces are recorded for times $t < t_{eq}$ while the mixing-chamber temperature cools from T_i to T_{eq} (before the green dot) and then slow relaxation of $f(t,T_{eq})$ and $D(t,T_{eq})$ for longer times $t > t_{eq}$. The traces are normalized according to $\delta f \equiv [f(t,T) - f(0,T_i)]/[f(\infty,T_{eq}) - f(0,T_i)]$ and $\delta D \equiv [D(t,T) - D(0,T_i)]/[D(\infty,T_{eq}) - D(0,T_i)]$ for comparison at different temperatures T_{eq}. (**C**) Measured temperature dependence of $\tau_f(T)$ and $\tau_D(T)$, the relaxation time constants for frequency and for dissipation as defined in the text.

mometers approach T_{eq}. More importantly, the subsequent changes after the thermometers equilibrate, $f(t,T_{eq})$ and $D(t,T_{eq})$, are measured. Data from five representative experiments are shown in Fig. 2, A and B, with each trace offset by 5000 s for clarity. In Fig. 2A, the vertical axis represents the percentage of the total frequency change during each experiment. In Fig. 2B, it represents the percentage of the equivalent total dissipation change. The green circles denote the time t_{eq} at which the mixing-chamber temperature equilibrates. Though for the initial $t < t_{eq}$ part of each trace both $f(t)$ and $D(t)$ change rapidly with temperature, their slopes change sharply at t_{eq}, indicating that the solid inside the TO maintains thermal equilibrium with the mixing chamber.

Before the "supersolid" signature appears, Fig. 2, A and B, reveal that these relaxation rates are independent of temperature and less than 100 s. But below this temperature, they begin to increase rapidly. The time constants for relaxation processes in f and D, $\tau_f(T)$ and $\tau_D(T)$, are indicated schematically in Fig. 2, A and B. They are measured by fitting the exponential $f(t) = C_1 - C_2 \exp(-t/\tau_f(T))$ and $D(t) = C_3 - C_4 \exp(-t/\tau_D(T))$ to each trace for times $t > t_{eq} = 0$. Both $\tau_f(T)$ and $\tau_D(T)$ increase rapidly on indistinguishable trajectories (Fig. 2C), indicating that the ultraslow relaxation processes in f and D are intimately linked. Such ultraslow dynamics in the "supersolid" state have also been observed elsewhere (*20*, *32*, *33*). It is difficult to reconcile any of these effects with thermal relaxation in a superfluid. Therefore, a better understanding of the relaxation dynamics of amorphous solid ^{4}He is required.

We first examine the relation between the relaxation dynamics of dissipation and the frequency shift as both approach their long-time equilibrium states. In the relevant experiment [fig. S2 (*31*)], the ^{4}He sample is cooled to 17 mK and then equilibrated for a time $t > 20{,}000$ s to achieve an unchanging state. It is then heated abruptly to a temperature T, and the subsequent relaxation dynamics in both $f(t,T)$ and $D(t,T)$ are monitored. The resulting time dependence of dissipation $D(t,T)$ is shown in Fig. 3A. At short times after temperature stabilization, the dissipation increases slightly (dark blue in Fig. 3A). However, these dissipative processes are actually very far out of equilibrium. As time passes, the dissipation slowly increases on a trajectory indicated by the transition from the blue line representing $D(t,T)$ at $t \sim 50$ s to the dark red line representing $D(t,T)$ at ~5000 s. In the same experiment, the time dependence of $f(t,T)$ is also measured (Fig. 3B). It differs from that of $D(t,T)$; at shortest times after stabilization at T the frequency has already changed greatly from its lowest-temperature value (Fig. 3B). This means that much of the frequency change responds immediately to the mixing-chamber temperature change (and therefore also that rapid thermal equilibrium always exists between the sample and the mixing-chamber thermometer). The subsequent evolution of the remaining component of the frequency shift exhibits an ultraslow reduction in f, as indicated by the transition from the blue line at $t \sim 50$ s to the dark red line representing $t \sim 5000$ s in Fig. 3B. These data illustrate how the slowing relaxation dynamics within $D(t,T)$ and $f(t,T)$ are synchronized in such samples of solid ^{4}He.

They also imply that thermal hysteresis should occur when temperatures are swept faster than the relevant time constants in Fig. 3, A and B. In Fig. 3C, swept-temperature measurements on the same sample show that thermal hysteresis occurs in both $f(t,T)$ and $D(t,T)$, with their long-time equilibrium values (solid circles) falling within the hysteresis loops as expected.

These extraordinary relaxation dynamics in $D(t,T)$ and $f(t,T)$ are unexpected in the context of a familiar superfluid. But effects analogous to these are seen during the freeze-out of excitations at a dielectric glass transition (*34*).Thus, the phenomenology of solid ^{4}He might also be due to a freeze-out of an ensemble of excitations within the solid (*22*). Indeed, there have been numerous proposals (*27*–*30*) that solid ^{4}He is a "superglass"—some form of granular superfluid within an amorphous solid.

To examine such hypotheses, we consider the total rotational susceptibility $\chi(\omega,T)$ of the TO plus solid ^{4}He sample (*22*). A classic Debye susceptibility describing the freeze-out of an ensemble of identical excitations with decay time $\tau(T)$ is $\chi_D^{-1}(\omega, T) = g_0/(1 - i\omega\tau(T))$. For solid ^{4}He, g_0/ω_0^2 would represent the rotational inertia associated with the relevant excitations. Their "back action" on the TO would appear in the total susceptibility as

$$\chi^{-1}(\omega, T) = K - I\omega^2 - i\gamma\omega - g_0/(1 - i\omega\tau(T)) \quad (1)$$

where γ is the intrinsic damping constant of the TO ($\omega_0 = \sqrt{K/I} = 2\pi f_0$; Fig. 1). The effect of changing the temperature can be captured entirely by the Debye term χ_D^{-1}, whose real and imaginary parts are

$$\Re[\chi_D^{-1}(T)] = \frac{g_0}{1 + \omega_0^2\tau^2}$$

$$\Im[\chi_D^{-1}(T)] = \frac{g_0\omega_0\tau}{1 + \omega_0^2\tau^2} \quad (2A, 2B)$$

at $\omega = \omega_0$. Thus, when one susceptibility component changes due to the $\tau(T)$ term, the other

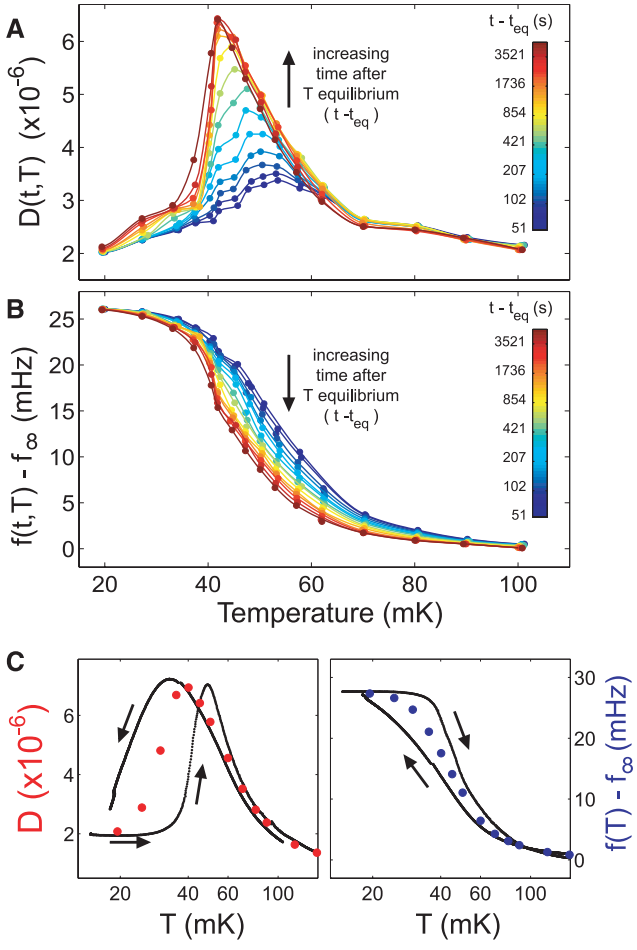

Fig. 3. Measured time evolution of (**A**) $D(t,T)$ and (**B**) $f(t,T)$ for the abrupt warming experiment described in the text and fig. S2. The data are colored circles and the lines are smooth interpolations, intended as a guide to the eye. The dark blue lines represent $D(t,T)$ and $f(t,T)$ at $t \sim 50$ s, while the dark red lines represent $D(t,T)$ and $f(t,T)$ at ~5000 s. (**C**) Thermal hysteresis in the dynamical response as shown by the black curves in $D(T)$ (left) and in $f(T)$ (right), with the direction of the temperature change indicated by a black arrow. The data indicated by red and blue circles were acquired after waiting $t >> 5 \times 10^3$ s at each temperature as the dynamical response [of (A) and (B)] asymptotically approached the infinite-time limit.

must always change in a quantitatively related manner. Such changes are measurable because

$$\frac{2(f_0 - f(T))}{f_0} = \frac{1}{I\omega_0^2}\Re[\chi_D^{-1}(T)]$$

$$D(T) - D_\infty = \frac{1}{I\omega_0^2}\Im[\chi_D^{-1}(T)] \qquad (3A, 3B)$$

within the Debye model with suitable approximations (*31*); $D_\infty \equiv \gamma/I\omega_0$. Moreover a well-defined characteristic temperature T^* for such a susceptibility occurs when $\omega_0\tau(T^*) = 1$; both the $f(T)$ slope and the dissipation $D(T)$ achieve their maxima at T^* (Fig. 1).

In Fig. 4A (left), we show a fit of Eq. 3B to the measured $D(T)$ as a red line, while Fig. 4A (right) shows the resulting prediction from Eq. 3A for $f(T)$ as the blue line. Comparison to the measured $f(T)$ (solid blue circles) shows that this Debye susceptibility is inconsistent with the relation between $D(T)$ and $f(T)$. Nevertheless, as the relaxation processes of $D(t,T)$ and $f(t,T)$ are synchronized (Fig. 3), there must be an intimate relation between $\Re[\chi^{-1}(t,T)]$ and $\Im[\chi^{-1}(t,T)]$. To study this relation, one should replot the data from Fig. 3, A and B, in the complex plane with axes defined by $\Im[\chi_D^{-1}]$ and $\Re[\chi_D^{-1}]$ [a Davidson-Cole (D-C) plot (*31*)]. This is a classic technique in which departures of the data from the Debye model appear as geometric features that can reveal characteristics of the underlying physical mechanism linking $\Re[\chi^{-1}(t,T)]$ and $\Im[\chi^{-1}(t,T)]$.

We therefore plot $\Delta D(T) = D(T) - D_\infty$ versus $\frac{2(f_0 - f(T))}{f_0}$ in Fig. 4B. It reveals that, instantaneously upon warming, the D-C plot is a symmetric elliptical curve, whereas after several thousand seconds, the response has evolved into the skewed D-C curve more familiar from studies of the dielectric glass transition (*34*). But the maximum frequency shift expected from the maximum observed dissipation within the Debye susceptibility (vertical dashed lines) is again far too small. Moreover, no temperature equilibration lag between the solid ^{4}He sample and the mixing chamber could generate the complex dynamics reported in Fig. 4 because, for any given frequency shift, a wide variety of different dissipations are observed [see supporting online material (SOM) text].

A simple superfluid transition is inconsistent with all these observations because there should be no synchronized dissipation peak associated with $f(T)$ (Figs. 1 and 4) and no ultraslow dynamics in $f(t,T)$ and $D(t,T)$ (Figs. 2 and 3). Indeed, these phenomena are more reminiscent of the characteristics of a glass transition (*34*). Nevertheless, a simple freeze-out of excitations described by a Debye susceptibility is also quantitatively inconsistent because the dissipation peak is far too small to explain the observed frequency shift (Fig. 4A). Thus, when considered in combination with implications of the blocked annulus experiments (*9*, *16*), our observations motivate a new hypothesis in which amorphous solid ^{4}He is a supersolid, but one whose superfluid phase-stiffness can be controlled by the freeze-out of an ensemble of excitations within the solid.

Within such a model, generation of excitations at higher temperatures would suppress superfluid phase stiffness. The complex relaxation dynamics (Figs. 3 and 4) would reveal the excitation freeze-out processes. Further, the anomalously large frequency shifts (Fig. 4) would occur predominantly because of superfluid phase stiffness appearing after excitation freezing. Such a model might also explain the diverse phenomenology of solid ^{4}He. For example, the ω dependence of T^* (*13*) would occur because T^* is the temperature for which $\tau(T^*)\omega = 1$. The shear modulus stiffening (*21*) would occur because of the freeze-out of motion of these excitations, and T^* would increase with ^{3}He concentration (*8*, *11*) because, with pinning, higher temperatures would be required to achieve the excitation rate $\tau(T^*)\omega_0 = 1$. Finally, sample-preparation effects (*10*, *12*) and different responses from different TO types would occur because the amorphousness allowing these excitations would depend on annealing and TO design.

Independent of these hypotheses, important new features of solid ^{4}He are revealed here. We find synchronized ultraslow relaxation dynamics of dissipation $D(T)$ and a component of frequency shift of $f(T)$ in TOs containing amorphous solid ^{4}He (Fig. 3). Such phenomena are reminiscent of the glassy freeze-out of an ensemble of excitations and inconsistent with a simple superfluid transition. Nevertheless, although the evolutions of $f(T)$ and $D(T)$ are linked dynamically, the situation is also inconsistent with the simple excitation freezing transition because there is an anomalously large frequency shift (Fig. 4). One possible explanation is that solid ^{4}He is not a supersolid and that the appropriate rotational susceptibility model for its transition will be identified eventually. But if superfluidity is the correct interpretation of blocked annulus experiments (*9*, *16*), then our results indicate that solid ^{4}He supports an exotic supersolid in which the glassy freeze-out at T^* of an unknown excitation within the amorphous solid controls the superfluid phase stiffness. Such a state could be designated a "superglass."

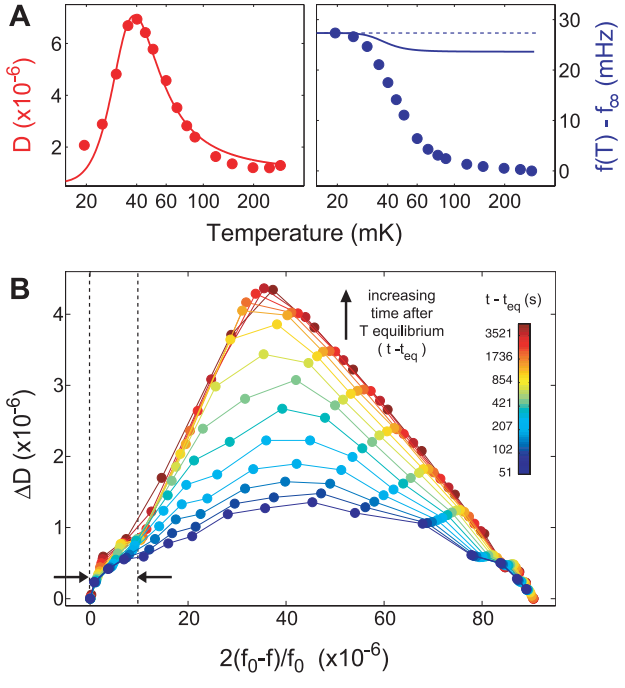

Fig. 4. (**A**) Comparison of equilibrated $D(T)$ and $f(T)$ data with simple Debye model of susceptibility in Eq. 1. The long-time equilibrated data $D(T)$ (left) and $f(T)$ (right) are plotted as filled circles. The dashed line indicates f_0. The solid curves represent the predicted relation between the susceptibilities for a simple glassy freeze-out transition. Although the dissipation $D(T)$ can be fit reasonably well by this model (*22*), the magnitude of the frequency shift that is then predicted is markedly smaller than observed. (**B**) Time-dependent D-C plot. This is a parametric plot of the data shown in Fig. 3, A and B, made by removing the explicit dependence on temperature, with axes defined by $\Im[\chi_D^{-1}]$ and $\Re[\chi_D^{-1}]$ (Eq. 3). The vertical dashed lines indicate the maximum value of $2(f_0 - f)/f_0$ that would be predicted by the Debye susceptibility (Eq. 1), given the peak height of $\Delta D = D - D_\infty$ (*31*).

References and Notes

1. D. Thouless, *Ann. Phys.* **52**, 403 (1969).
2. A. F. Andreev, I. M. Lifshitz, *Sov. Phys. JETP* **29**, 1107 (1969).
3. L. Reatto, *Phys. Rev.* **183**, 334 (1969).
4. G. V. Chester, *Phys. Rev. A* **2**, 256 (1970).
5. A. J. Leggett, *Phys. Rev. Lett.* **25**, 1543 (1970).
6. M. W. Meisel, *Physica B* **178**, 121 (1992).
7. D. R. Tilley, J. Tilley, *Superfluidity and Superconductivity* (IOP, Bristol, UK, ed. 3, 1990).
8. E. Kim, M. H. W. Chan, *Nature* **427**, 225 (2004).
9. E. Kim, M. H. W. Chan, *Science* **305**, 1941 (2004).
10. A. C. Clark, J. T. West, M. H. W. Chan, *Phys. Rev. Lett.* **99**, 135302 (2007).
11. E. Kim *et al.*, *Phys. Rev. Lett.* **100**, 065301 (2008).
12. A. S. C. Rittner, J. D. Reppy, *Phys. Rev. Lett.* **97**, 165301 (2006).
13. Y. Aoki, J. C. Graves, H. Kojima, *Phys. Rev. Lett.* **99**, 015301 (2007).
14. A. Penzev, Y. Yasuta, M. Kubota, *J. Low Temp. Phys.* **148**, 677 (2007).
15. M. Kondo, S. Takada, Y. Shibayama, K. Shirahama, *J. Low Temp. Phys.* **148**, 695 (2007).
16. A. S. C. Rittner, J. D. Reppy, *Phys. Rev. Lett.* **101**, 155301 (2008).
17. S. Sasaki, R. Ishiguro, F. Caupin, H. J. Maris, S. Balibar, *Science* **313**, 1098 (2006).
18. J. Day, J. Beamish, *Phys. Rev. Lett.* **96**, 105304 (2006).
19. M. W. Ray, R. B. Hallock, *Phys. Rev. Lett.* **100**, 235301 (2008).

20. A. C. Clark, J. D. Maynard, M. H. W. Chan, *Phys. Rev. B* **77**, 184513 (2008).
21. J. Day, J. Beamish, *Nature* **450**, 853 (2007).
22. Z. Nussinov, A. V. Balatsky, M. J. Graf, S. A. Trugman, *Phys. Rev. B* **76**, 014530 (2007).
23. A. F. Andreev, *JETP Lett.* **85**, 585 (2007).
24. P. W. Anderson, *Nat. Phys.* **3**, 160 (2007).
25. L. Pollet *et al.*, *Phys. Rev. Lett.* **98**, 135301 (2007).
26. C.-D. Yoo, A. Dorsey, *Phys. Rev. B* **79**, 100504 (2009).
27. M. Boninsegni *et al.*, *Phys. Rev. Lett.* **96**, 105301 (2006).
28. J. Wu, P. Phillips, *Phys. Rev. B* **78**, 014515 (2008).
29. J. Bossy, J. V. Pearce, H. Schober, H. R. Glyde, *Phys. Rev. B* **78**, 224507 (2008).
30. G. Biroli, C. Chamon, F. Zamponi, *Phys. Rev. B* **78**, 224306 (2008).
31. Materials and methods are available as supporting material on *Science* Online.
32. Y. Aoki, M. C. Keiderling, H. Kojima, *Phys. Rev. Lett.* **100**, 215303 (2008).
33. V. N. Grigor'ev *et al.*, *Phys. Rev. B* **76**, 224524 (2007).
34. B. K. P. Scaife, *Principles of Dielectrics* (Clarendon, Oxford, UK, 1989).
35. We acknowledge and thank J. Beamish, M. W. H. Chan, A. Clark, A. Dorsey, M. Graf, E. Mueller, S. Nagel, M. Paalanen, R. E. Packard, J. Parpia, J. D. Reppy, A. S. Rittner, J. Saunders, J. P. Sethna, and Wm. Vinen for helpful discussions and communications. These studies were initiated under NSF grant DM-0434801 and are now partially supported under grant DMR-0806629 and by Cornell University; B.H. acknowledges support by the Natural Sciences and Engineering Research Council of Canada. M.Y. acknowledges support from the Japan Society for the Promotion of Science. Work at Los Alamos was supported by the U.S. Department of Energy.

Supporting Online Material

www.sciencemag.org/cgi/content/full/324/5927/632/DC1
Materials and Methods
SOM Text
Figs. S1 to S6
References

9 December 2008; accepted 18 March 2009
10.1126/science.1169512

Competition for Light Causes Plant Biodiversity Loss After Eutrophication

Yann Hautier,[1]* Pascal A. Niklaus,[1,2] Andy Hector[1]

Human activities have increased the availability of nutrients in terrestrial and aquatic ecosystems. In grasslands, this eutrophication causes loss of plant species diversity, but the mechanism of this loss has been difficult to determine. Using experimental grassland plant communities, we found that addition of light to the grassland understory prevented the loss of biodiversity caused by eutrophication. There was no detectable role for competition for soil resources in diversity loss. Thus, competition for light is a major mechanism of plant diversity loss after eutrophication and explains the particular threat of eutrophication to plant diversity. Our conclusions have implications for grassland management and conservation policy and underscore the need to control nutrient enrichment if plant diversity is to be preserved.

Fertilization experiments (*1*–*4*) and studies of nutrient deposition in terrestrial ecosystems (*5*) show that increases in the availability of nitrogen (*5*, *6*), phosphorus (*7*), and other nutrients—both alone and in combination (*1*, *4*)—usually increase primary productivity and decrease plant diversity. Given that anthropogenic activity has doubled global phosphorus liberation and plant-available nitrogen during the past 50 years (*8*, *9*), and that nutrient inputs are predicted to be one of the three major drivers of biodiversity loss this century (*10*), understanding the mechanisms responsible for diversity loss after eutrophication will be important for the development of effective conservation policies (*11*).

Most of the hypotheses proposed to explain the reduction in plant diversity after eutrophication focus on changes in competition (*12*–*15*). Fertilization may increase the strength of competition generally—that is, both above and below ground (*15*)—or it could increase the strength of aboveground competition for light only: an asymmetric process due to the directional supply of this resource (*13*, *14*). The hypothesis of increased competition for light (*14*) predicts that as productivity increases, availability of light to plants in the understory is reduced, leading to their exclusion by faster-growing or taller species that preempt this directionally supplied resource (*16*, *17*). Surprisingly, 35 years after these alternative hypotheses were suggested, there is no consensus on the role of competition as a mechanism of plant diversity loss after eutrophication (*18*, *19*).

To test whether diversity loss after eutrophication is due to increased competition for light, we added light to the understory of fertilized grassland communities—a manipulation inspired by competition experiments with algae (*20*, *21*). A key advance of our approach relative to earlier work (*22*) is that it restores light to the species in the lower canopy that are thought to decrease in diversity as a result of deeper shading after the increase in aboveground productivity caused by eutrophication. We conducted a glasshouse experiment that combined addition of fertilizer and supplementary light in a fully factorial design. The 32 experimental plant communities were pregrown in the field for 4 years (*23*) before they were extracted with intact soil blocks and moved to the glasshouse. For generality, the communities comprised four different sets of six species (*23*) that had similar levels of diversity and, as we show, responded similarly to the experimental treatments.

Light was added to the understory of each treated community using a system of three fluorescent tubes that were raised as the canopy grew (Fig. 1). Reflectors were placed above the fluorescent tubes to direct light into the understory and to prevent it from shining up onto the underside of the leaves of the taller species. To keep conditions other than light and fertilization as similar as possible, we installed the same system of fluorescent tubes in communities without supplementary light, but in this case reflectors were placed above and below the tubes to form a closed chamber from which the light could not escape. With this system, we were able to experimentally manipulate light in the understory while holding other conditions (such as temperature) constant. Aboveground biomass was harvested twice a year during 2006 and 2007 to coincide with the cutting regimes typical of European meadows, and other key variables (including belowground biomass production, canopy height, availability of light in the understory, soil pH, and plant diversity) were regularly monitored (*24*).

After 2 years of treatment, fertilization had increased net aboveground biomass production and decreased diversity (*24*). During the second year, fertilization significantly increased production from an average of 356 ± 39 g m^{-2} (mean ± SEM) per harvest in the control communities to 450 ± 39 g m^{-2} in the fertilized treatment (Fig. 2A and table S1). The percentage of photosynthetically active radiation in the understory of the fertilized plots (5 ± 4%) was significantly lower than for the controls (13 ± 4%) (Fig. 2B). Notably, when increased production was accompanied by decreased light in the understory, fertilization significantly reduced species richness (Fig. 2C): On average, 2.6 species were lost in the fertilization treatment relative to the control, around one-third of the original species richness. This loss of diversity after eutrophication is consistent with longer-term field studies (*1*, *5*).

When applied together with fertilization, the additional understory light compensated for the increased shading caused by the greater aboveground biomass production and generated levels of understory light (12 ± 4%) that were indistinguishable from those in the control plots (13 ± 4%) (Fig. 2B and table S1). Supplementing understory light in the fertilization treatment to levels similar to the control plots prevented the loss of

[1]Institute of Environmental Sciences, University of Zürich, Winterthurerstrasse 190, CH-8057 Zürich, Switzerland. [2]Institute of Plant Sciences, ETH Zürich, Universitätstrasse 2, CH-8092 Zürich, Switzerland.

*To whom correspondence should be addressed. E-mail: yhautier@uwinst.uzh.ch